

Waves at a fluid-solid interface: Explicit versus implicit formulation of boundary conditions using a discontinuous Galerkin method

Khemraj Shukla, José M. Carcione, Jan S. Hesthaven, and Elizabeth L'heureux

Citation: *The Journal of the Acoustical Society of America* **147**, 3136 (2020); doi: 10.1121/10.0001170

View online: <https://doi.org/10.1121/10.0001170>

View Table of Contents: <https://asa.scitation.org/toc/jas/147/5>

Published by the *Acoustical Society of America*

READ NOW!

JASA
THE JOURNAL OF THE
ACOUSTICAL SOCIETY OF AMERICA

Special Issue:
Acoustic Localization

Waves at a fluid-solid interface: Explicit versus implicit formulation of boundary conditions using a discontinuous Galerkin method

Khemraj Shukla,^{1,a)} José M. Carcione,² Jan S. Hesthaven,³ and Elizabeth L'heureux⁴

¹Center of Computation and Visualization, Brown University, 180 George Street, Providence, Rhode Island 02906, USA

²Istituto Nazionale di Oceanografia e di Geofisica Sperimentale (OGS), Borgo Grotta Gigante 42c, 34010 Sgonico, Trieste, Italy

³Computational Mathematics and Simulation Sciences (MCSS), École Polytechnique Fédérale de Lausanne, Lausanne, Switzerland

⁴Complex Imaging Group, BP America, Houston, Texas 77079, USA

ABSTRACT:

An accurate solution of the wave equation at a fluid-solid interface requires a correct implementation of the boundary condition. Boundary conditions at fluid-solid interface require continuity of the normal component of particle velocity and traction, whereas the tangential components vanish. A main challenge is to model interface waves, namely, the Scholte and leaky Rayleigh waves. This study uses a nodal discontinuous Galerkin (dG) finite-element method with the medium discretized using an unstructured uniform triangular meshes. The natural boundary conditions in the dG method are implemented by (1) using an explicit upwind numerical flux and (2) by using an implicit penalty flux and setting the modulus of rigidity of the acoustic medium to zero. The accuracy of these methods is evaluated by comparing the numerical solutions with analytical ones, with source and receiver at and away from the interface. The study shows that the solutions obtained from the explicit and implicit boundary conditions provide the correct results. The stability of the dG scheme is determined by the numerical flux, which also implements the boundary conditions by unifying the numerical solution at shared edges of the elements in an energy stable manner.

© 2020 Acoustical Society of America. <https://doi.org/10.1121/10.0001170>

(Received 26 December 2019; revised 12 March 2020; accepted 12 April 2020; published online 4 May 2020)

[Editor: Assad Anshuman Oberai]

Pages: 3136–3150

I. INTRODUCTION

The accurate computation of wave fields in realistic Earth models is an ongoing challenge in local and global seismology. The problem becomes more challenging in the presence of fluid-solid interfaces. Of particular interest are applications in geophysics, i.e., marine seismic exploration concerning the ocean bottom or global Earth seismology, using earthquake-generated seismic waves as a probing field, involving the core-mantle-boundary (CMB) and inner-core-boundary (ICB). The physics of the fluid is modeled by the acoustic wave equation by assuming that the density of the fluid is independent of pressure, with non-zero bulk modulus, but zero rigidity (μ) or shear. The propagation in the solid is governed by the elastic wave equation, which assumes that the medium has finite bulk and rigidity moduli. Alternatively, the acoustic wave equation is obtained by setting μ to zero in the elastic approximation.

In a fluid-solid setup, there exist two interface waves: first, the “Scholte waves” that mainly travel into the liquid (Cagniard, 1962), and second, the leaky-Rayleigh wave (Ash and Paige, 1985). The latter wave decays with depth in the solid while it behaves as a propagating mode in the fluid (Ash and Paige, 1985) with characteristics similar to the head waves. Surprisingly, the amplitude of the leaky-

Rayleigh mode in fluid increases as it propagates away from the interface (Farnell, 1970).

The main physical aspects of the interface waves are discussed in Glorieux *et al.* (2002), Glorieux *et al.* (2001), and Padilla *et al.* (1999). In what follows, “acoustic-elastic” and “fluid-solid” are used interchangeably. In subsequent sections, the bulk velocities of the longitudinal waves in fluid and solid are represented by c_f and c_p , respectively, the shear-wave velocity of the solid is represented by c_s , and the phase velocity of the leaky Rayleigh wave, free Rayleigh waves in the solid and Scholte wave are denoted by c_{pR} , c_R , and c_{Sc} , respectively. The findings of Glorieux *et al.* (2002), Glorieux *et al.* (2001), and Padilla *et al.* (1999) are summarized as:

- (1) In the case of $c_f < c_s < c_p$, the stiff solid condition, the leaky-Rayleigh wave propagates with a phase velocity (c_{pR}) slightly lower than c_s and leaks energy in the form of the head wave.
- (2) In the case of $c_s < c_f < c_p$, the soft solid condition, Padilla *et al.* (1999) state that the leaky Rayleigh mode travels in the fluid without dissipation as it is described by a real root. This non-physical observation is refuted by Glorieux *et al.* (2001) with the argument that the root corresponding to the leaky Rayleigh mode is incorrectly identified.
- (3) If the density of the fluid ρ_f is close to zero, the leaky Rayleigh wave becomes a free Rayleigh wave.

^{a)}Electronic mail: rajexplo@gmail.com

- (4) In the case of a large contrast in the acoustic impedance of the solid and fluid, the phase velocity of the Scholte wave c_{Sc} is close to c_f .
- (5) For the case of a soft solid $c_s < c_f < c_p$, the phase velocity of the Scholte wave is less than c_f and the wave becomes more localized.
- (6) In the two-dimensional (2D) case, the Scholte wave travels without attenuation whereas in three dimensions the dissipation of energy is caused by geometrical spreading.

Hence, for a stiff solid, it holds that $c_{Sc} < c_R < c_f < c_{pR} < c_s < c_p$. The domain of existence of the leaky Rayleigh mode is described by the Rayleigh window defined by the angle between the front of the Rayleigh wave and the interface (Carcione and Helle, 2004).

A variety of numerical methods have been used to solve the acousto-elastic system. The discretization is performed on (a) first-order system of partial differential equations (PDEs) in the stress-velocity formulation, or (b) in its original form of displacement, described by a system of second-order PDEs. A detailed discussion on the numerical methods, adopted for simulation of interface waves in a fluid-solid setup, is discussed in a recent study by Carcione *et al.* (2018). The first to model the interface was Stephen (1983). He used a second-order finite-difference method to solve the elastic wave equation and treated the boundary condition by approximating the interface with a transition zone where the velocity increases gradually. Stephen also treated the boundary condition by setting $c_s = 0$ in the acoustic media but obtained erroneous results. A spectral finite element method was used by Komatitsch *et al.* (2000) who treated the boundary conditions explicitly. The study by Komatitsch *et al.* (2000) does not show the propagation of interface waves and lacks the comparison between numerical and analytical solutions. van Vossen *et al.* (2002) used an explicit method based on finite differences, where only five grid points per wavelength are required for an accurate modeling. Zhang (2004) used an integral-based approach to model the boundary conditions explicitly with a domain discretized by unstructured meshes. The studies presented by van Vossen *et al.* (2002) and Zhang (2004) do not show the propagation of interface waves (Scholte and leaky Rayleigh waves) and also do not show the accuracy of the numerical solutions by comparison to the analytical solution. Carbajal-Romero *et al.* (2013) used a boundary element method to simulate the body and Scholte waves, excluding the leaky Rayleigh wave, and validated their results by comparing against solutions obtained by using a discrete wave-number method and a spectral-element method. Chaljub *et al.* (2003) solve the system for a heterogeneous fluid-solid sphere but did not simulate the interface waves. Madec *et al.* (2009) solved the system by using a high-order finite element method and primarily simulated the body waves but do not consider the interface waves. De Basabe and Sen (2014) modeled the Scholte waves and compared the solutions obtained with several algorithms such as finite

differences and spectral-element methods, which show limited accuracy. They concluded that the single-grid method has spurious modes in the fluid subdomain, but they do not show any results obtained by an explicit method.

Recently, Carcione *et al.* (2018) simulated the interface waves using a direct-grid method, based on Chebyshev spatial differentiation, by incorporating natural boundary conditions using implicit and explicit approaches. In the implicit method, the natural boundary condition is incorporated by setting $c_s = 0$ in the acoustic medium (fluid). The explicit method is based on a domain decomposition technique (Carcione, 2014). They concluded that the implicit method gives erroneous numerical results by comparing the numerical and analytical solutions, whereas the explicit method was found to work.

Unlike the methods discussed above, all of which recover the numerical solution globally, we consider the discontinuous Galerkin (dG) method. In the dG method, the global solution is obtained by unifying the solution at the shared edges of the elements by using a weak operator, known as a numerical flux (Hesthaven and Warburton, 2007). The boundary and interface conditions are incorporated in the scheme through this operator. The numerical flux determines the stability of the numerical scheme and thus ensures a correct implementation of the interface boundary conditions. For a linear problem, the flux can be computed explicitly by solving a Riemann problem on the interior boundary of each element (Wilcox *et al.*, 2010), discretizing the acousto-elastic domain, resulting in an upwind flux. The computation of the upwind flux is expensive as it involves the eigen-decomposition, which becomes more cumbersome for anisotropic media and the extension is non-trivial. To circumvent this problem, Ye *et al.* (2016) proposed an implicit method to compute the numerical flux by adding a penalty term to the central flux (jump in the value of the field variables in the direction normal to the edge of the element), which eventually stabilizes the numerical scheme. In this study, we compute the numerical solutions using both fluxes, upwind and penalized central fluxes, and show that in both cases, the dG method captures the interface waves accurately.

The paper is organized as follows. Section II outlines the acousto-elastic system and Sec. III reviews the dispersion equation for interface waves. Section IV describes the system of equations in matrix form. Section V formulates the dG scheme for a coupled acoustic-elastic system, and Sec. VI presents the results. In Sec. VII, we offer a few concluding remarks.

II. SYSTEM OF EQUATIONS DESCRIBING ACOUSTIC-ELASTIC WAVES

The 2D velocity-stress equations for elastic wave propagation in the (x_1, x_3) plane can be expressed by the following:

- (i) Euler-Newton equations

$$\dot{v}_1 = \frac{1}{\rho} \left(\frac{\partial \sigma_{11}}{\partial x_1} + \frac{\partial \sigma_{13}}{\partial x_3} \right), \tag{1}$$

$$\dot{v}_3 = \frac{1}{\rho} \left(\frac{\partial \sigma_{13}}{\partial x_1} + \frac{\partial \sigma_{33}}{\partial x_3} \right), \tag{2}$$

where v_1 and v_3 are the particle velocities along the x and z axis, σ_{11} , σ_{33} , and σ_{13} are stress components, and ρ is the density. A dot above a variable denotes the time derivative.

(ii) Constitutive equations

$$\dot{\sigma}_{11} = (\lambda + \mu) \left(\frac{\partial v_1}{\partial x_1} + \frac{\partial v_3}{\partial x_3} \right) + \mu \left(\frac{\partial v_1}{\partial x_1} - \frac{\partial v_2}{\partial x_3} \right) + f_{11}, \tag{3}$$

$$\dot{\sigma}_{33} = (\lambda + \mu) \left(\frac{\partial v_1}{\partial x_1} + \frac{\partial v_3}{\partial x_3} \right) - \mu \left(\frac{\partial v_1}{\partial x_1} - \frac{\partial v_3}{\partial x_3} \right) + f_{33}, \tag{4}$$

$$\dot{\sigma}_{13} = \mu \left(\frac{\partial v_1}{\partial x_3} + \frac{\partial v_3}{\partial x_1} \right) + f_{13}, \tag{5}$$

where λ and μ are the Lamé constants, and $\mathbf{f} = [f_{11}, f_{33}, f_{13}]^T$ are moment-tensor components. In this work, \mathbf{f} is assumed to be the product of compactly supported spatial functions (specifically Dirac delta functions) and a Ricker wavelet in the time domain. In 2D, $\lambda = \rho(c_p^2 - 2c_s^2)$ and $\mu = \rho c_s^2$.

III. THE DISPERSION EQUATION

The dispersion equation is obtained by implementing the continuity of the normal components of the displacement and stress at the interface. This is expressed as (Carcione *et al.*, 2018; Carcione and Helle, 2004; Glorieux *et al.*, 2002; Glorieux *et al.*, 2001; Scholte, 1942)

$$S(q) = 4\sqrt{(1-q)(1-aq)} - (2-q)^2 - \left(\frac{\rho_f}{\rho} \right) q^2 \sqrt{\frac{1-aq}{1-bq}}, \tag{6}$$

where $q = v^2/c_s^2$, $a = c_s^2/c_L^2$, and $b = c_s^2/c_f^2$ with v being the complex velocity of the interface waves.

The dispersion equation of the elastic Rayleigh wave is obtained by taking $\rho_f = 0$ in Eq. (6). The Riemann surface of $S(q)$ has eight sheets, corresponding to different choices of the signs of the complex roots $\sqrt{1-q}$, $\sqrt{1-aq}$, and $\sqrt{1-bq}$ (Ansell, 1972). In the lossless case, the roots of the Scholte and the leaky Rayleigh waves are real and complex, respectively. These surface waves are a superposition of inhomogeneous elastic waves and the attenuation vector makes an angle of 90° with respect to the propagation vector. The Scholte wave attenuates in the direction perpendicular to the interface, while the leaky Rayleigh wave attenuates along the interface. The Scholte waves travel without attenuation in 2D lossless media, whereas in three-dimensional (3D) media, the energy of Scholte waves decays due to geometrical spreading. The

energy of the leaky Rayleigh wave decays both in 2D and 3D lossless media.

The leaky wave exists only for a stiff solid bottom since the shear-wave velocity in the solid is smaller than the sound velocity in the fluid. The leaky Rayleigh wave becomes the Rayleigh wave as the density of the liquid approaches zero. Therefore, for a stiff bottom, the Rayleigh wave is not the Scholte wave if the density of the liquid goes to zero (Carcione and Helle, 2004). For soft bottoms, the shear-wave velocity in the solid is smaller than the sound velocity in the fluid. Moreover, the Scholte wave becomes the free Rayleigh wave if the density of the liquid tends to zero (Rauch, 1980). The existence of the free Rayleigh wave is unconditional, whereas the leaky Rayleigh wave exists only for stiff bottoms. In this case, the leaky Rayleigh wave has a velocity slightly lower than the body-wave shear velocity and the Scholte wave velocity is lower than the velocity in the liquid (Carcione *et al.*, 2018; Carcione and Helle, 2004). The velocity of the Scholte wave approaches the velocity of the liquid as the stiffness of the solid increases.

IV. SYMMETRIC FORM OF THE SYSTEM OF EQUATION IN MATRIX FORM

Equations (1)–(5) can be rewritten as a symmetric hyperbolic system of PDEs using the Voigt notation

$$\rho \frac{\partial \mathbf{v}}{\partial t} = \sum_{i \in \{1,3\}} \mathbf{A}_i^T \frac{\partial \boldsymbol{\sigma}}{\partial x_i}, \tag{7}$$

$$\mathbf{C}^{-1} \frac{\partial \boldsymbol{\sigma}}{\partial t} = \sum_{i \in \{1,3\}} \mathbf{A}_i \frac{\partial \mathbf{v}}{\partial x_i} + \mathbf{f}, \tag{8}$$

where

$$\mathbf{C} = \begin{bmatrix} \lambda + 2\mu & \lambda & 0 \\ \lambda & \lambda + 2\mu & 0 \\ 0 & 0 & \mu \end{bmatrix},$$

$$\mathbf{C}^{-1} = \frac{1}{\lambda\mu + 4\mu^2} \begin{bmatrix} \lambda + 2\mu & -\lambda & 0 \\ -\lambda & \lambda + 2\mu & 0 \\ 0 & 0 & \frac{4\mu^2 + \mu\lambda}{\mu} \end{bmatrix},$$

$$\mathbf{v} = [v_1, v_3]^T, \quad \boldsymbol{\sigma} = (\sigma_{11}, \sigma_{33}, \sigma_{13}),$$

$$\mathbf{A}_1 = \begin{bmatrix} 1 & 0 \\ 0 & 0 \\ 0 & 1 \end{bmatrix}, \quad \mathbf{A}_3 = \begin{bmatrix} 0 & 0 \\ 0 & 1 \\ 1 & 0 \end{bmatrix}, \quad \text{and}$$

$$\mathbf{f} = [f_{11}, f_{33}, f_{13}]^T$$

Note that \mathbf{C} is symmetric and positive-definite. Matrices \mathbf{A}_1 and \mathbf{A}_2 are constant but ρ , \mathbf{C} and \mathbf{C}^{-1} may vary spatially.

Combining Eqs. (7) and (8) yields

$$\mathbf{Q} \frac{\partial \mathbf{q}}{\partial t} + \nabla \cdot (\mathbf{A} \mathbf{q}) = \mathbf{f}, \tag{9}$$

where

$$\mathbf{Q} = \left[\begin{array}{c|c} \mathbf{C}_{3 \times 3}^{-1} & \mathbf{0} \\ \hline \mathbf{0} & \rho \end{array} \right], \quad \mathbf{q} = [\sigma_{11}, \sigma_{33}, \sigma_{13}, v_1, v_3]^T, \quad \text{and}$$

$$\mathbf{A} = [\mathbf{A}_{12}, \mathbf{A}_{21}]^T \quad \text{with}$$

$$\mathbf{A}_{12} = \left[\begin{array}{cc} \mathbf{A}_1 & \mathbf{0}_{3 \times 3} \\ \mathbf{0}_{2 \times 2} & \mathbf{A}_1^T \end{array} \right] \quad \text{and} \quad \mathbf{A}_{21} = \left[\begin{array}{cc} \mathbf{A}_3 & \mathbf{0}_{3 \times 3} \\ \mathbf{0}_{2 \times 2} & \mathbf{A}_3^T \end{array} \right].$$

V. A DG FORMULATION FOR ACOUSTO-ELASTIC WAVE PROPAGATION

We assume that the domain Ω is triangulated by a mesh Ω_h that consists of elements D^k , which are images of a reference element \hat{D} under the local affine mapping,

$$\mathbf{x}^k = \Phi^k \hat{\mathbf{x}}, \tag{10}$$

where $\mathbf{x}^k = \{x^k, y^k\}$ denote the physical coordinates on D^k and $\hat{\mathbf{x}} = \{\hat{x}, \hat{y}\}$ denote coordinates on the reference element. We denote the determinant of the Jacobian of Φ^k as J .

Solutions over each element D^k are approximated from a local approximation space $V_h(D^k)$, which is defined as a composition of the mapping Φ^k and a reference approximation space $V_h(\hat{D})$

$$V_h(D^k) = \Phi^k \circ V_h(\hat{D}). \tag{11}$$

The global approximation space $V_h(\Omega_h)$ is defined as

$$V_h(\Omega_h) = \bigoplus_k V_h(D^k), \tag{12}$$

where \bigoplus represents the direct sum. We take $V_h(\hat{D}) = P^N(\hat{D})$, with $P^N(\hat{D})$ being the space of polynomials of total degree N on the reference simplex. In two dimensions, P^N on a triangle is

$$P^N(\hat{D}) = \{\hat{x}^i \hat{y}^j, 0 \leq i + j \leq N\}. \tag{13}$$

The L^2 inner product and norm over D^k is defined as

$$\begin{aligned} (\mathbf{g}, \mathbf{h}) &= \int_{D^k} \mathbf{g} \cdot \mathbf{h} \, dx = \int_{\hat{D}} \mathbf{g} \cdot \mathbf{h} J \, d\hat{\mathbf{x}}, \\ \|\mathbf{g}\|_{L^2 \Omega}^2 &= (\mathbf{g}, \mathbf{g})_{L^2(D^k)}, \end{aligned}$$

where \mathbf{g} and \mathbf{h} are vector-valued real functions. Global L^2 -products and squared norms are defined as the sum of local L^2 -inner products and squared norms over each element. The L^2 -inner product and norm over the boundary ∂D^k of an element are similarly defined as

$$\begin{aligned} \langle \mathbf{u}, \mathbf{v} \rangle_{L^2(\partial D^k)} &= \int_{\partial D^k} \mathbf{u} \cdot \mathbf{v} \, dx = \sum_{f \in \partial D^k} \int_{\hat{f}} \mathbf{u} \cdot \mathbf{v} J^f \, d\hat{\mathbf{x}}, \\ \|\mathbf{u}\|_{L^2(\partial D^k)}^2 &= \langle \mathbf{u}, \mathbf{u} \rangle, \end{aligned}$$

where J^f is the Jacobian of the mapping from a reference face \hat{f} to a physical face f of an element.

Let f be a face of element D^k with neighboring element $D^{k,+}$ and unit outward normal \mathbf{n} . Let u be a piecewise smooth function with discontinuities across element interfaces. We define the interior value u^- and exterior value u^+ on face f of D^k ,

$$u^- = u|_{f \cap \partial D^{k,-}}, \quad u^+ = u|_{f \cap \partial D^{k,+}}.$$

The jump and average of a scalar function $u \in V_h(\Omega_h)$ over f are then defined as

$$[[u]] = u^+ - u^-, \quad \{\{u\}\} = \frac{u^+ + u^-}{2},$$

respectively. Jumps and averages of vector-valued functions $\mathbf{u} \in \mathbb{R}^m$ and matrix-valued functions $\tilde{\mathbf{S}} \in \mathbb{R}^{m \times n}$ are defined component-wise,

$$([[\tilde{\mathbf{S}}]])_i = [[\mathbf{u}_i]], \quad 1 \leq i \leq m \quad ([[\tilde{\mathbf{S}}]])_{ij} = [[\tilde{\mathbf{S}}]].$$

The system of equations [Eq. (9)] is linear and the dG scheme used here is in strong form, obtained after integrating the residual by parts twice (Hesthaven and Warburton, 2007). The strong form also imposes the differentiable and continuity requirements on the solutions and thus justifies the term ‘‘strong.’’ The requirements of continuity and differentiability are readily achieved for a linear system.

The strong formulation of Eq. (9) on an element D^k is

$$\begin{aligned} \int_{D^k} \mathbf{Q} \frac{\partial \mathbf{q}}{\partial t} \cdot \mathbf{p} \, dx + \int_{D^k} (\nabla \cdot \mathbf{A} \mathbf{q}) \cdot \mathbf{p} \, dx \\ + \int_{\partial D^k} (\mathbf{n} \cdot ((\mathbf{A} \mathbf{q})^* - \mathbf{A}^- \mathbf{q}^-)) \cdot \mathbf{p} \, dx = \int_{D^k} \mathbf{f} \cdot \mathbf{p} \, dx \end{aligned}$$

for all $\mathbf{p} \in V_h(\Omega_h)$, (14)

where $(\mathbf{A} \mathbf{q})^*$ is the numerical flux. The choice of the flux will determine the method of implementation of boundary conditions, i.e., explicitly or implicitly.

A. Explicit scheme

To compute the upwind flux, we solve a Riemann problem at shared edges of each element, corresponding to an elastic-elastic, acoustic-acoustic, acoustic-elastic, and elastic-acoustic interfaces. The Riemann problem to solve Eq. (14) is defined as

$$\mathbf{q}_0(\mathbf{x}) = \begin{cases} \mathbf{q}^- & \text{if } \mathbf{n} \cdot \mathbf{x} < 0 \\ \mathbf{q}^+ & \text{if } \mathbf{n} \cdot \mathbf{x} > 0. \end{cases} \tag{15}$$

The solution of Eq. (15) is described separately for elastic-elastic, acoustic-acoustic, and elastic-acoustic or acoustic elastic-interfaces.

1. Elastic-elastic interfaces

Equation (9) is written as

$$\mathbf{Q} \frac{\partial \mathbf{q}}{\partial t} + \frac{\partial \mathbf{A}_{12} \mathbf{q}}{\partial x_1} + \frac{\partial \mathbf{A}_{21} \mathbf{q}}{\partial x_3} = \mathbf{f}. \quad (16)$$

In the remainder of this section, $\mathbf{n} := \mathbf{n}^-$ denotes the outward interface unit normal vector and the flux in the normal direction is $\mathbf{A}_n \mathbf{q}$ with $\mathbf{A}_n = n_1 \mathbf{A}_{12} + n_3 \mathbf{A}_{21}$. To construct an upwind flux requires the computations of the characteristics of the hyperbolic system defined in Eq. (9). To compute the characteristics, we consider the eigen-decomposition of $\mathbf{Q}^{-1} \mathbf{A}_n$ as

$$\mathbf{Q}^{-1} \mathbf{A} = \mathbf{R} \mathbf{\Lambda} \mathbf{R}^{-1} \quad (17)$$

with $\mathbf{\Lambda} = \text{diag}(-c_p, -c_s, 0, c_s, c_p)$ and the j th column of \mathbf{R} is an eigenvector of $\mathbf{Q}^{-1} \mathbf{A}$. For each wave speed c_i in our system, the Rankine-Hugonite jump condition is expressed as

$$-c_i \mathbf{Q}(\mathbf{q}^m - \mathbf{q}^p) + \mathbf{A}_n(\mathbf{q}^m - \mathbf{q}^p) = 0, \quad (18)$$

where \mathbf{q}^m and \mathbf{q}^p are states in the negative and positive normal directions, travelling with speed c_i , across the discontinuity. Matrices \mathbf{Q} and \mathbf{A}_n are evaluated in the region where mode c_i travels, denoted by “-” and “+.” The Riemann problem has four unknown states ($\mathbf{q}^a, \mathbf{q}^b, \mathbf{q}^c, \mathbf{q}^d$) as shown in Fig. 1. A full set of Rankine-Hugonite jump conditions is given as

$$c_p^- \mathbf{Q}^-(\mathbf{q}^- - \mathbf{q}^a) + \mathbf{A}_n^-(\mathbf{q}^- - \mathbf{q}^a) = 0, \quad (19)$$

$$c_s^- \mathbf{Q}^-(\mathbf{q}^a - \mathbf{q}^b) + \mathbf{A}_n^-(\mathbf{q}^a - \mathbf{q}^b) = 0, \quad (20)$$

$$\mathbf{A}_n^- \mathbf{q}^b - \mathbf{A}_n^+ \mathbf{q}^c = 0, \quad (21)$$

$$-c_s^+ \mathbf{Q}^+(\mathbf{q}^a - \mathbf{q}^b) + \mathbf{A}_n^+(\mathbf{q}^c - \mathbf{q}^d) = 0, \quad (22)$$

$$-c_p^+ \mathbf{Q}^+(\mathbf{q}^d - \mathbf{q}^+) + \mathbf{A}_n^+(\mathbf{q}^d - \mathbf{q}^+) = 0. \quad (23)$$

Using the definitions of the eigenvalues and eigenvectors of $(\mathbf{Q}^-)^{-1} \mathbf{A}^-$ and $(\mathbf{Q}^+)^{-1} \mathbf{A}^+$, we obtain

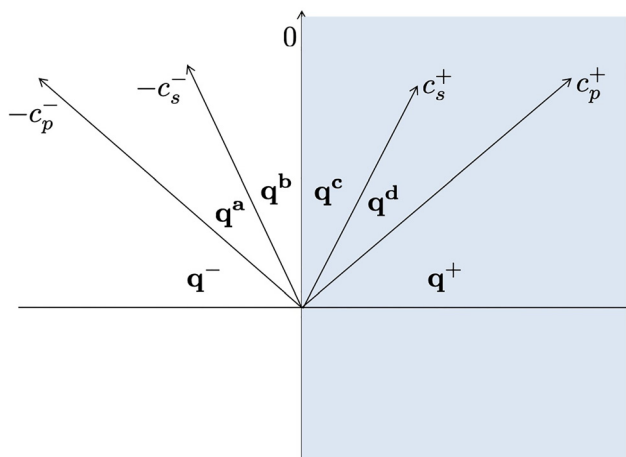


FIG. 1. (Color online) Rankine-Hugonite jump conditions in the Riemann's problem.

$$\begin{aligned} \mathbf{q}^- - \mathbf{q}^a &= \alpha_1 \mathbf{r}_1^-, \\ \mathbf{q}^a - \mathbf{q}^b &= \alpha_2 \mathbf{r}_2^- + \alpha_3 \mathbf{r}_3^-, \\ \mathbf{q}^c - \mathbf{q}^d &= \alpha_7 \mathbf{r}_7^+ + \alpha_8 \mathbf{r}_8^+, \\ \mathbf{q}^d - \mathbf{q}^+ &= \alpha_9 \mathbf{r}_9^+. \end{aligned}$$

Thus, the upwind numerical flux $(\mathbf{A}_n \mathbf{q})^*$ is defined as (Hesthaven and Warburton, 2007).

$$\begin{aligned} \mathbf{n} \cdot ((\mathbf{A}_n \mathbf{q})^* - \mathbf{A}^- \mathbf{q}^-) &= \alpha_1 c_p^- \mathbf{Q}^- \mathbf{r}_1^- + \alpha_2 c_s^- \mathbf{Q}^- \mathbf{r}_2^- \\ &\quad + \alpha_3 c_s^- \mathbf{Q}^- \mathbf{r}_3^-. \end{aligned} \quad (24)$$

The expression of α_1 , α_2 , and α_3 is derived in detail by Wilcox *et al.* (2010). After substituting α_1 , α_2 , and α_3 into Eq. (24), we recover

$$\begin{aligned} \mathbf{n} \cdot ((\mathbf{A}_n \mathbf{q})^* - \mathbf{A}^- \mathbf{q}^-) &= \frac{\mathbf{n} \cdot [[\boldsymbol{\sigma}]] + \rho^+ c_p^+ [[\mathbf{v}]]}{\rho^+ c_p^+ + \rho^- c_p^-} \\ &\quad \times \left[\frac{\lambda^- \mathbf{I} + 2\mu^- \mathbf{n} \otimes \mathbf{n}}{\rho^- c_p^- \mathbf{n}} \right] \\ &\quad - \frac{1}{(\rho^- c_s^- + \rho^+ c_s^+)} \\ &\quad \times \left[\frac{2\mu^- \text{sym}(\mathbf{n} \otimes (\mathbf{n} \times (\mathbf{n} \times [[\boldsymbol{\sigma}]]))}{\rho^- c_s^- \mathbf{n} \times (\mathbf{n} \times [[\boldsymbol{\sigma}]])} \right] \\ &\quad - \frac{\rho^+ c_s^+}{\rho^- c_s^- + \rho^+ c_s^+} \\ &\quad \times \left[\frac{2\mu^- \text{sym}(\mathbf{n} \otimes (\mathbf{n} \times (\mathbf{n} \times [\mathbf{v}])))}{\rho^- c_s^- \mathbf{n} \times (\mathbf{n} \times [\mathbf{v}])} \right]. \end{aligned} \quad (25)$$

2. Acoustic-acoustic interface

Acoustic-acoustic interfaces are characterized by $\mu^- = \mu^+ = 0$ and \mathbf{q} reduces to $\hat{\mathbf{q}} = [\sigma_{11}, \sigma_{33}, v_1, v_3]$. By using relation $\partial \sigma_{13} / \partial t = \mu[(\partial v_1 / \partial x_3) + (\partial v_3 / \partial x_1)]$, we can solve the Riemann problem to compute $\hat{\mathbf{q}}$ and keep the number of variables the same as in the case of the elastic-elastic interface. Rankine-Hugonite jump conditions for acoustic-acoustic interface are given as

$$c_p^- \mathbf{Q}^-(\mathbf{q}^- - \mathbf{q}^a) + \mathbf{A}_n^-(\mathbf{q}^- - \mathbf{q}^a) = 0, \quad (26)$$

$$\mathbf{A}_n^- \mathbf{q}^a - \mathbf{A}_n^+ \mathbf{q}^b = 0, \quad (27)$$

$$-c_p^+ \mathbf{Q}^+(\mathbf{q}^b - \mathbf{q}^+) + \mathbf{A}_n^+(\mathbf{q}^b - \mathbf{q}^+) = 0. \quad (28)$$

Following the same approach as in the elastic-elastic case, the flux for the acoustic-acoustic interface is

$$\mathbf{n} \cdot ((\mathbf{A}_n \mathbf{q})^* - \mathbf{A}^- \mathbf{q}^-) = \frac{\mathbf{n} \cdot [[\boldsymbol{\sigma}]] + \rho^+ c_p^+ [[\mathbf{v}]]}{\rho^+ c_p^+ + \rho^- c_p^-} \left[\frac{\lambda^- \mathbf{I}}{\rho^- c_p^- \mathbf{n}} \right]. \quad (29)$$

3. Elastic-acoustic and acoustic-elastic interfaces

For the elastic-acoustic interface ($\mu^- \neq 0$ and $\mu^+ = 0$), the solutions to the Riemann problem satisfy the Rankine-Hugonite jump conditions

$$c_p^- \mathcal{Q}^-(q^- - q^a) + A_n^-(q^- - q^a) = 0, \tag{30}$$

$$c_s^- \mathcal{Q}^-(q^a - q^b) + A_n^-(q^a - q^b) = 0, \tag{31}$$

$$A_n^- q^b - A_n^+ q^c = 0, \tag{32}$$

$$-c_p^+ \hat{\mathcal{Q}}^+(\hat{q}^c - \hat{q}^+) + \hat{A}_n^+(\hat{q}^c - \hat{q}^+) = 0, \tag{33}$$

where $\hat{q} = [\sigma_{11}, \sigma_{33}, v_1, v_3]^T$ and $\hat{\mathcal{Q}} = \mathcal{Q}|_{\mu=0}$. The resulting numerical flux incorporates an upwind term from an incoming c_p characteristic and a boundary term from an incoming c_s characteristic (Wilcox et al., 2010). The boundary condition for an incoming c_s characteristic is expressed as (Wilcox et al., 2010)

$$s \cdot v^- - 2c_s^- s \cdot \sigma n = s \cdot v^+, \tag{34}$$

where s is the tangential vector along the interface. Solving Eqs. (30)–(33) as in the elastic-elastic case and imposing the boundary condition [Eq. (34)] weakly, the numerical flux for the elastic-acoustic interface becomes

$$\begin{aligned} n \cdot ((Aq)^* - A^- q^-) &= \frac{n \cdot [[\sigma]] + \rho^+ c_p^+ [[v]]}{\rho^+ c_p^+ + \rho^- c_p^-} \\ &\times \begin{bmatrix} \lambda^- I + 2\mu^- n \otimes n \\ \rho^- c_p^- n \end{bmatrix} \\ &- \frac{1}{\rho^- c_s^-} \\ &\times \begin{bmatrix} 2\mu^- \text{sym}(n \otimes (n \times (n \times [[\sigma]]))) \\ \rho^- c_s^- n \times (n \times [[\sigma]]) \end{bmatrix}. \end{aligned} \tag{35}$$

Equation (35) may be interpreted as an elastic-elastic flux (25) for $\mu^+ = 0$. Using the same logic, the flux for the acoustic-elastic interface ($\mu^- = 0$ and $\mu^+ \neq 0$) is

$$n \cdot ((Aq)^* - A^- q^-) = \frac{n \cdot [[\sigma]] + \rho^+ c_p^+ [[v]]}{\rho^+ c_p^+ + \rho^- c_p^-} \begin{bmatrix} \lambda^- I \\ \rho^- c_p^- n \end{bmatrix}. \tag{36}$$

The flux for the acoustic-elastic interface [Eq. (36)] is the same as that of the acoustic-acoustic interface [Eq. (29)]. Thus, for the explicit scheme, the flux in Eqs. (25), (29), (35), and (36) is appropriately chosen by evaluating the values of μ^- and μ^+ of the medium.

B. Implicit scheme

The implicit scheme requires $\mu=0$ in the numerical scheme. The dG scheme must be consistent locally as well

as globally. The solid-solid, fluid-fluid, and solid-fluid boundary conditions are expressed as

$$v^+ - v^- = 0 \quad \text{and} \quad n \cdot \sigma^+ - n \cdot \sigma^- = 0 \quad \text{on } \Gamma_{SS}, \tag{37a}$$

$$n \cdot (v^\pm - \hat{v}^\pm) = 0 \quad \text{and} \quad n \cdot \sigma^\pm - n \cdot \hat{\sigma}^\pm = 0 \quad \text{on } \Gamma_{SF} \quad \text{and} \quad \Gamma_{FS}, \tag{37b}$$

$$\hat{v}^+ - \hat{v}^- = 0 \quad \text{and} \quad \hat{\sigma}^+ - \hat{\sigma}^- = 0 \quad \text{on } \Gamma_{FF}. \tag{37c}$$

To derive the implicit scheme, the matrix form of the acoustic wave equation is required and can be expressed as

$$\hat{\mathcal{Q}} \frac{\partial \hat{q}}{\partial t} + \nabla \cdot (\hat{A} \hat{q}) = \hat{f}, \tag{38}$$

where

$$\hat{\mathcal{Q}} = \begin{bmatrix} \lambda & \mathbf{0} \\ \mathbf{0} & \rho \mathbf{I}_{3 \times 3} \end{bmatrix} \quad \text{and}$$

$$\hat{q} = [\hat{\sigma}, v_1, v_2] \quad \text{with} \quad \hat{\sigma} = -\lambda \hat{E}$$

where \hat{E} is the longitudinal strain.

The dG scheme in strong form for Eq. (38) is

$$\begin{aligned} \int_{D^k} \hat{\mathcal{Q}} \frac{\partial \hat{q}}{\partial t} \cdot \hat{p} dx + \int_{D^k} (\nabla \cdot \hat{A} \hat{q}) \cdot \hat{p} dx \\ + \int_{\partial D^k} (n \cdot ((\hat{A} \hat{q})^* - \hat{A}^- \hat{q}^-)) \cdot \hat{p} dx \\ = \int_{D^k} \hat{f} \cdot \hat{p} dx \quad \text{for all } \hat{p} \in V_h(\Omega_h). \end{aligned} \tag{39}$$

To derive an implicit scheme, we consider a Lax-Friedrich flux (Hesthaven and Warburton, 2007), i.e.,

$$n \cdot (Aq^*) = n_x \{ \{ Aq \} \} + n_y \{ \{ Aq \} \} + \frac{c_{\max}}{2} [q], \tag{40}$$

where c_{\max} is the maximum phase velocity of the modes present in the system.

Substituting Eq. (40) in Eq. (14), the surface term is recovered as

$$n \cdot ((Aq)^* - A^- q^-) = \frac{1}{2} [[Aq]] + \frac{c_{\max}}{2} [q]. \tag{41}$$

In Eq. (41), the first term, $(1/2)[[Aq]]$ is responsible for the interface boundary conditions in Eqs. (37a)–(37c), whereas the second term $(c_{\max}/2)[q]$ is a penalty term that stabilizes the scheme. Implementation of the flux in Eq. (40) for the acousto-elastic system with $\mu=0$ will produce wrong results as the numerical scheme in Eq. (14) with the flux in Eq. (41) is consistent for purely elastic or acoustic systems, but not for a coupled acoustic-elastic system (Wilcox et al., 2010).

To accurately incorporate the interface conditions at solid-solid, fluid-fluid, solid-fluid, and fluid-solid boundaries

In Eqs. (14) and (39), we express the dG formulation for the acoustic and elastic conditions as follows:

$$\int_{D_S^k} \mathbf{Q} \frac{\partial \mathbf{q}}{\partial t} \cdot \mathbf{p} dx + \int_{D_S^k} (\nabla \cdot \mathbf{A} \mathbf{q}) \cdot \mathbf{p} dx + \frac{1}{2} \int_{\partial D_{SS}^k} [[\mathbf{A}_n \mathbf{q}]]_{SS} \cdot \mathbf{p} dx + \frac{1}{2} \int_{\partial D_{SF}^k} [[\mathbf{A}_n \mathbf{q}]]_{SF} \cdot \mathbf{p} dx = \int_{D^k} \mathbf{f} \cdot \mathbf{p} dx \text{ for all } \mathbf{p} \in V_h(\Omega_h), \quad (42)$$

$$\int_{D_F^k} \hat{\mathbf{Q}} \frac{\partial \hat{\mathbf{q}}}{\partial t} \cdot \hat{\mathbf{p}} dx + \int_{D_F^k} (\nabla \cdot \hat{\mathbf{A}} \hat{\mathbf{q}}) \cdot \hat{\mathbf{p}} dx + \frac{1}{2} \int_{\partial D_{FF}^k} [[\hat{\mathbf{A}}_n \hat{\mathbf{q}}]]_{FF} \cdot \hat{\mathbf{p}} dx + \frac{1}{2} \int_{\partial D_{FS}^k} [[\hat{\mathbf{A}}_n \hat{\mathbf{q}}]]_{FS} \cdot \hat{\mathbf{p}} dx = \int_{D_F^k} \hat{\mathbf{f}} \cdot \hat{\mathbf{p}} dx \text{ for all } \hat{\mathbf{p}} \in V_h(\Omega_h), \quad (43)$$

where

$$\begin{aligned} [[\mathbf{A}_n \mathbf{q}]]_{SS} &= (\mathbf{A}_n \mathbf{q})^+ - (\mathbf{A}_n \mathbf{q})^-, \\ [[\mathbf{A}_n \mathbf{q}]]_{SF} &= \mathbf{T}^T (\hat{\mathbf{A}} \hat{\mathbf{q}})^+ - (\mathbf{A}_n \mathbf{q})^-, \\ [[\hat{\mathbf{A}}_n \hat{\mathbf{q}}]]_{FF} &= (\hat{\mathbf{A}}_n \hat{\mathbf{q}})^+ - (\hat{\mathbf{A}}_n \hat{\mathbf{q}})^-, \\ [[\hat{\mathbf{A}}_n \hat{\mathbf{q}}]]_{FS} &= \mathbf{T} (\mathbf{A}_n \mathbf{q})^+ - (\hat{\mathbf{A}}_n \hat{\mathbf{q}})^-, \end{aligned} \quad (44)$$

with the map $T : \mathbb{R}^5 \rightarrow \mathbb{R}^2$ given by (Ye et al., 2016)

$$T \mathbf{q} = \begin{bmatrix} \mathbf{n} \cdot \boldsymbol{\sigma} \cdot \mathbf{n} \\ (\mathbf{n} \cdot \mathbf{v}) \mathbf{n} \end{bmatrix} \text{ and } T^T \hat{\mathbf{q}} = \begin{bmatrix} (n \hat{\sigma}) \\ (\mathbf{n} \cdot \hat{\mathbf{v}}) \mathbf{n} \end{bmatrix},$$

where

$$T = \left[\begin{array}{ccc|cc} n_1 n_1 & n_3 n_2 & n_1 n_3 & \mathbf{0} & \\ \mathbf{0} & & & n_1 n_1 & n_1 n_3 \\ \hline & & & n_1 n_3 & n_2 n_3 \end{array} \right].$$

In Eqs. (42) and (43), the numerical fluxes are central fluxes that may be unstable. To stabilize these formulations, a penalization is used (Guo et al., 2019; Warburton, 2013; Ye et al., 2016). In this study, we used a penalization method of fluxes proposed by Ye et al. (2016). The penalized flux for the solid-solid is

$$F_E = \frac{1}{2} \int_{\partial D_{SS}^k} [[\mathbf{A}_n \mathbf{q}]]_{SS} \cdot \mathbf{p} dx + \frac{1}{2} \int_{\partial D_{SF}^k} [[\mathbf{A}_n \mathbf{q}]]_{SF} \cdot \mathbf{p} dx + \frac{\alpha}{2} \left[\int_{\partial D_{SS}^k} (\mathbf{A}_n^T [[\mathbf{A}_n \mathbf{q}]] \cdot \mathbf{p} dx + \int_{\partial D_{SF}^k} (\mathbf{A}_n^T [[\mathbf{A}_n \mathbf{q}]] \cdot \mathbf{p} dx \right], \quad (45)$$

where $\alpha > 0$.

Similarly, the penalized flux for the fluid-fluid and fluid-solid case is

TABLE I. Material properties.

Material	λ (GPa)	μ (GPa)	ρ (kg/m ³)
Water	2.25	0	1000
Plexiglass	4.3315	2.2799	1180
Glass	25.253	28.157	2500

$$F_A = \frac{1}{2} \int_{\partial D_{FF}^k} [[\hat{\mathbf{A}}_n \hat{\mathbf{q}}]]_{FF} \cdot \hat{\mathbf{p}} dx + \frac{1}{2} \int_{\partial D_{FS}^k} [[\hat{\mathbf{A}}_n \hat{\mathbf{q}}]]_{FS} \cdot \hat{\mathbf{p}} dx + \frac{\alpha}{2} \left[\int_{\partial D_{FF}^k} \hat{\mathbf{A}}_n^T [[\hat{\mathbf{A}}_n \hat{\mathbf{q}}]] \cdot \hat{\mathbf{p}} dx + \int_{\partial D_{FS}^k} \hat{\mathbf{A}}_n^T [[\hat{\mathbf{A}}_n \hat{\mathbf{q}}]] \cdot \hat{\mathbf{p}} dx \right]. \quad (46)$$

Substituting Eqs. (45) and (46) in Eqs. (42) and (43), we recover the final form of the penalty flux based implicit scheme

$$\int_{D_S^k} \mathbf{Q} \frac{\partial \mathbf{q}}{\partial t} \cdot \mathbf{p} dx + \frac{1}{2} \int_{\partial D_{SS}^k} [[\mathbf{A}_n \mathbf{q}]]_{SS} \cdot \mathbf{p} dx + \frac{1}{2} \int_{\partial D_{SF}^k} [[\mathbf{A}_n \mathbf{q}]]_{SF} \cdot \mathbf{p} dx + \frac{\alpha}{2} \left[\int_{\partial D_{SS}^k} (\mathbf{A}_n^T [[\mathbf{A}_n \mathbf{q}]] \cdot \mathbf{p} dx + \int_{\partial D_{SF}^k} (\mathbf{A}_n^T [[\mathbf{A}_n \mathbf{q}]] \cdot \mathbf{p} dx \right] = \int_{D^k} \mathbf{f} \cdot \mathbf{p} dx \text{ for all } \mathbf{p} \in V_h(\Omega_h), \quad (47)$$

$$\int_{D_F^k} \hat{\mathbf{Q}} \frac{\partial \hat{\mathbf{q}}}{\partial t} \cdot \hat{\mathbf{p}} dx + \frac{1}{2} \int_{\partial D_{FF}^k} [[\hat{\mathbf{A}}_n \hat{\mathbf{q}}]]_{FF} \cdot \hat{\mathbf{p}} dx + \frac{1}{2} \int_{\partial D_{FS}^k} [[\hat{\mathbf{A}}_n \hat{\mathbf{q}}]]_{FS} \cdot \hat{\mathbf{p}} dx + \frac{\alpha}{2} \left[\int_{\partial D_{FF}^k} \hat{\mathbf{A}}_n^T [[\hat{\mathbf{A}}_n \hat{\mathbf{q}}]] \cdot \hat{\mathbf{p}} dx + \int_{\partial D_{FS}^k} \hat{\mathbf{A}}_n^T [[\hat{\mathbf{A}}_n \hat{\mathbf{q}}]] \cdot \hat{\mathbf{p}} dx \right] = \int_{D_F^k} \hat{\mathbf{f}} \cdot \hat{\mathbf{p}} dx \text{ for all } \hat{\mathbf{p}} \in V_h(\Omega_h). \quad (48)$$

The choice of α affects the energy stability of the scheme shown in Eqs. (47) and (48) and damps under-resolved spurious components in the numerical solutions. A detailed discussion on the choice of α is presented by Chan (2018) and in Shukla et al. (2020). In the present study, we take $\alpha = 1$, but choosing $\alpha (> 0)$ naively results in a restrictive time-step (dt), which increases the runtime.

C. Time discretization

We employ the low-storage explicit Runge-Kutta (LSERK) method (Cockburn and Shu, 2001). The LSERK method is a single-step method but comprises five intermediate stages. LSERK is preferred over other methods as it saves memory at the cost of computation time. A stable

TABLE II. Velocities of body and surface waves.

Interface	c_f (m/s)	c_p (m/s)	c_s (m/s)	c_{Sc} (m/s)	c_{pR} (m/s)
Water-plexiglass	1500	2745	1390	1058	1363
Water-glass	1500	5712	3356	1496	3091

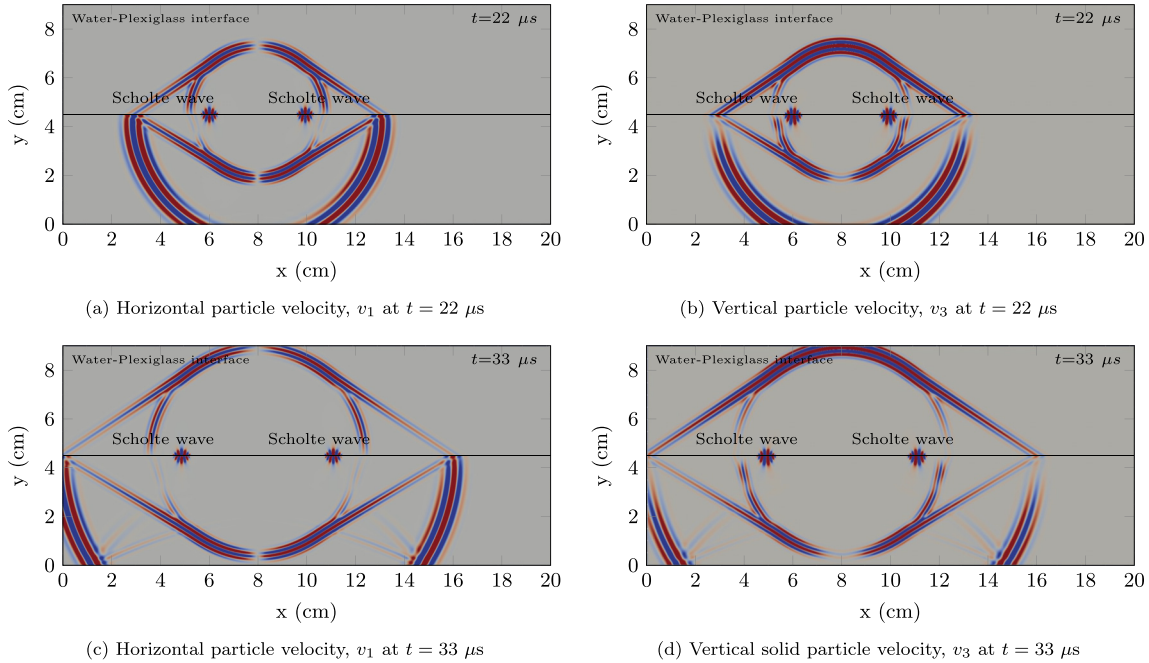


FIG. 2. (Color online) Snapshots of the simulated interface waves for a water-plexiglass interface, using explicit boundary-conditions, which show the horizontal and vertical particle velocities at 22 μs (a, b) and 33 μs (c, d). The source is located in the solid at 38.4 μm below the interface, and it is an explosion ($f_{11} = f_{33}$), with a central frequency of 500 kHz.

Courant–Friedrichs–Lewy condition, depending on the polynomial degree N , is derived by Cockburn and Shu (2001) and used here.

D. Forcing function

The forcing function f in Eq. (8) is the product of a Dirac delta in space (x_0) and a Ricker wavelet in time,

$$f = \delta(x - x_0)h(t), \tag{49}$$

where $h(t)$ is a wavelet, given by

$$h(t) = \exp \left[-2f_p^2(t - t_0)^2 \right] \cos [2\pi f_p(t - t_0)],$$

with f_p being the central peak frequency and $t_0 = 3/(4f_p)$. In subsequent sections, f_p is taken to be 500 kHz with a dilatational moment force ($f_{xx} = f_{zz}$ and $f_{xy} = 0$).

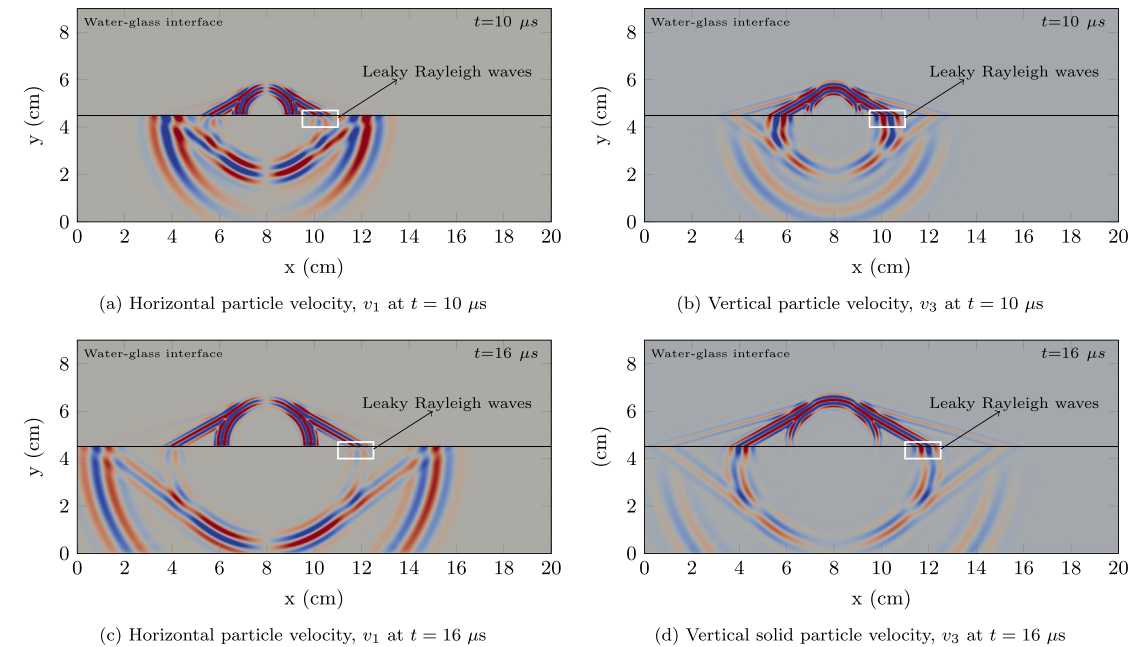


FIG. 3. (Color online) Snapshots of the simulated interface waves for a water-glass interface, using explicit boundary-conditions, which show the horizontal and vertical particle velocities at 10 μs (a, b) and 16 μs (c, d). The source is located in the solid at 38.4 μm below the interface, and it is an explosion ($f_{11} = f_{33}$), with a central frequency of 500 kHz.

VI. COMPUTATIONAL EXPERIMENTS

To perform the computational experiments, we consider a medium including water-plexiglass and water-glass interfaces. The material properties are given in Table I. The velocities of the body and surface or interface waves, computed from the dispersion relation [Eq. (6)], are given in Table II. The medium defined by the water-plexiglass combination represents the soft-solid system, whereas the water-glass interface is the stiff-solid condition. To determine the existence and evolution of the interface waves in soft and stiff solid conditions, we first solve the coupled acoustic-elastic system using the explicit numerical scheme, defined in Eq. (14) in Sec. V A.

Figure 2 shows snapshots of the particle velocities computed for the water-plexiglass or soft-solid condition. The size of the computational domain is [20 cm × 9 cm]. The minimum size of the edges of the equilateral triangles h , used to mesh the domain, in the x_1 and x_3 directions, are 0.37 mm (denoted as h_1) and 0.56 mm (denoted as h_3), respectively. The degree of the polynomial (N) is 2 and the time step dt used for time integration is 0.217 ns. The total number of elements, used for discretization, equals to 178 200 with 2 673 000 degrees of freedom. Figures 2(a) and 2(b) represent the snapshots of the horizontal (v_1) and

vertical (v_3) particle velocities at 22 ms. As discussed, the presence of the Scholte wave is observed and marked in Figs. 2(a) and 2(b). To visualize the evolution of the Scholte wave, Figs. 2(c) and 2(d) represent the particle velocities (v_1, v_2) at $t = 33 \mu\text{s}$. The Scholte wave moves to a distance of $\approx 1.164 \text{ cm}$ [Figs. 2(c) and 2(d)] at $t = 33 \mu\text{s}$ from 9.836 cm [Figs. 2(a) and 2(b)] measured at $t = 22 \mu\text{s}$. Thus, the velocity of the Scholte wave is equal to 1058.18 m/s. This is in agreement with the velocity computed from the dispersion relation, shown in Table II, with a relative error of 0.017%.

Figure 3 represents the snapshots of the horizontal (v_1) and vertical (v_3) particle velocities for the water-glass system, i.e., a stiff solid medium. The discretization parameters are the same as those used in Fig. 2 except dt , which is 0.104 ns. Figures 3(a) and 3(b) represent snapshot at $t = 10 \mu\text{s}$. The presence of a leaky Rayleigh mode is observed, also marked by a white box, at $x = 10 \text{ cm}$. To see the evolution of the leaky Rayleigh wave, the snapshots of horizontal and particle velocities computed at $t = 16 \mu\text{s}$ are shown in Figs. 3(c) and 3(d). The leaky Rayleigh mode is present $x = 11.855 \text{ cm}$. Thus, the velocity of the leaky Rayleigh mode computed is 3091.67 m/s, with a relative error of 0.022% as compared to the velocity obtained from the dispersion relation.

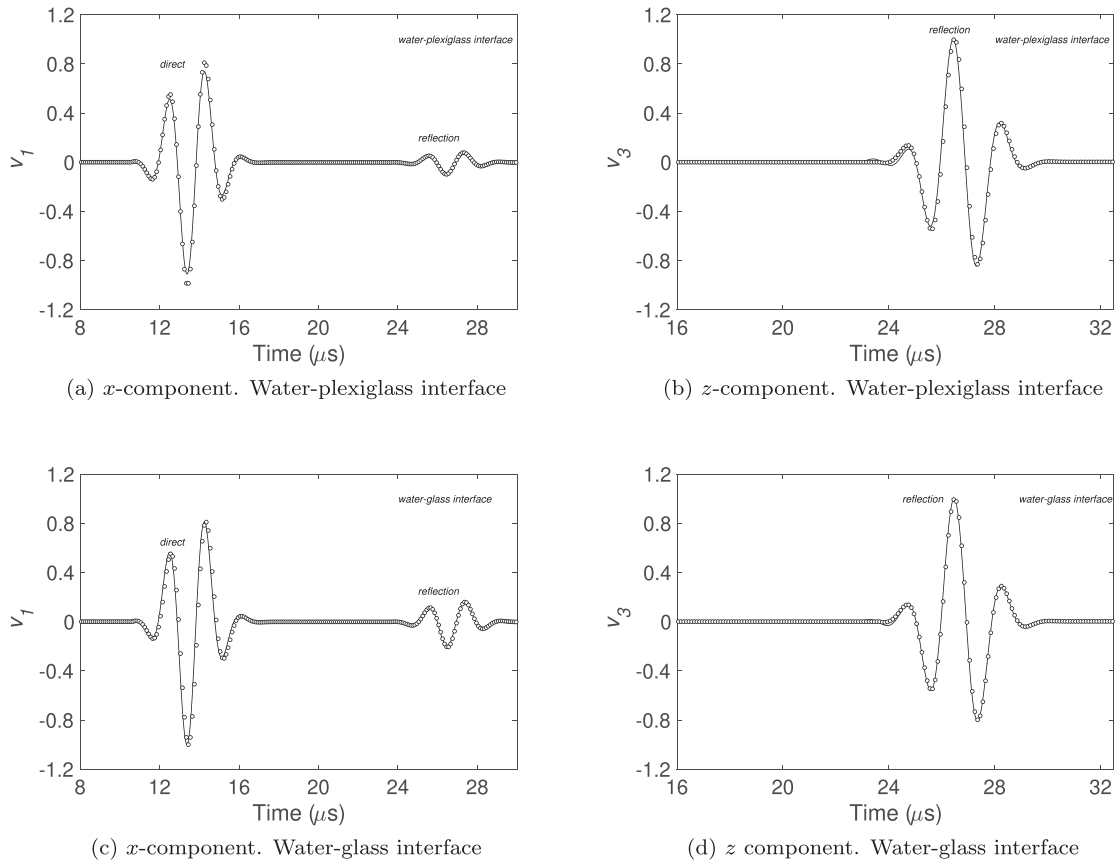


FIG. 4. Explicit boundary-condition: Simulation of the reflection response using an upwind flux, where the solid line and circles correspond to the numerical and analytical solutions, respectively. The figure shows the normalized particle-velocity components corresponding to water-plexiglass (a and b) and water-glass (c and d). Source and receiver are located in the fluid at 0.0158831 m above the interface and are separated by 0.016 m. The source is an explosion ($f_{11} = f_{33}$), with a central frequency of 500 kHz.

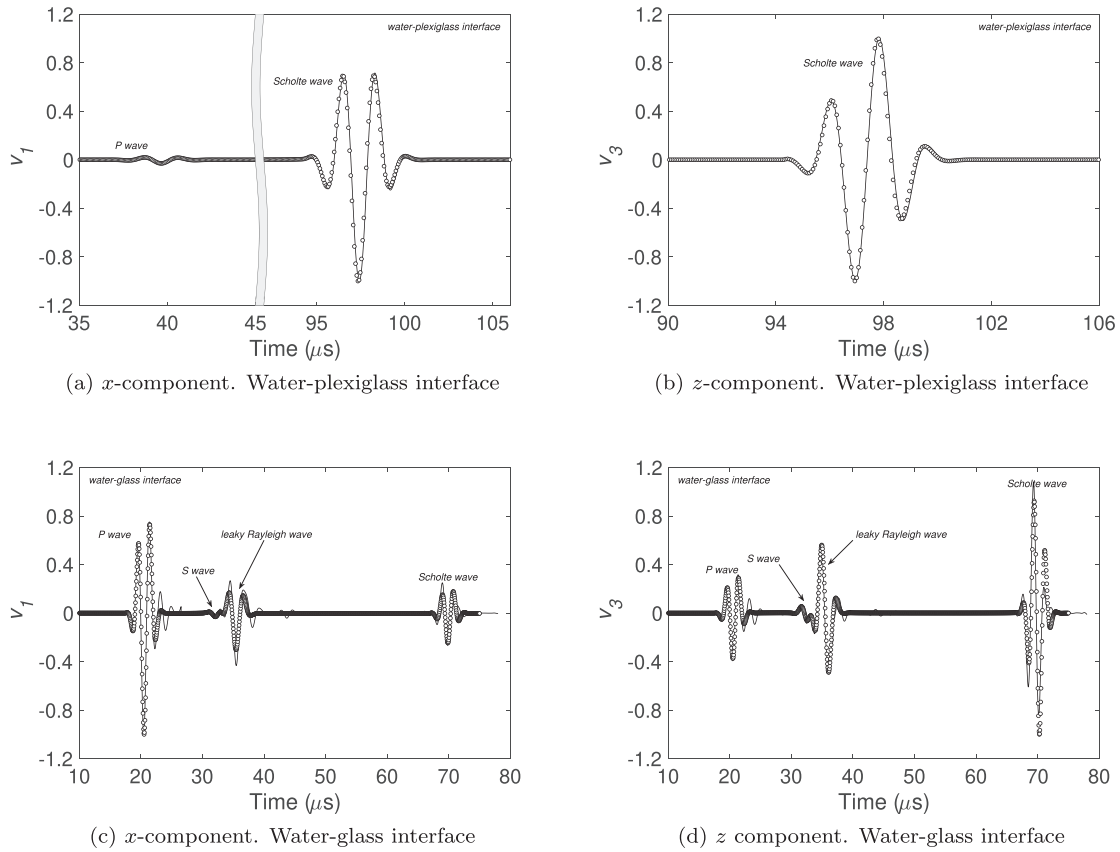


FIG. 5. Explicit boundary-condition: Simulation of interface-waves, where the solid line and dots correspond to the numerical solutions and analytical, respectively. The figure shows the normalized particle-velocity components corresponding to water-plexiglass (a and b) and water-glass (c and d). Source and receiver are both located in the solid at $38.4 \mu\text{m}$ below the interface, with a separation 0.1 m . The source is an explosion ($f_{11} = f_{33}$), with a central frequency of 500 kHz .

Figures 4–8 show the comparison of the numerical solution against the analytical solution obtained by Berg *et al.* (1994) using the method of Cagniard-de Hoop (de Hoop and Van der Hijden, 1983). Figure 4 shows the simulation of the reflection response using an upwind flux (explicit boundary conditions) with a polynomial degree $N=2$. Source and receiver are located in the fluid at 0.0158831 m above the interface and are separated by 0.016 m . The source is an

explosion with a central frequency of 500 kHz . The discretization parameters for the water-plexiglass and water-glass models are the same as those used for results shown in Figs. 2 and 3, respectively. The solid line and circles correspond to the numerical and analytical solutions, respectively. Figures 4(a) and 4(b) show the x_1 and x_3 components of the normalized particle velocities corresponding to the water-plexiglass model, respectively. Figures 4(c) and 4(d) show

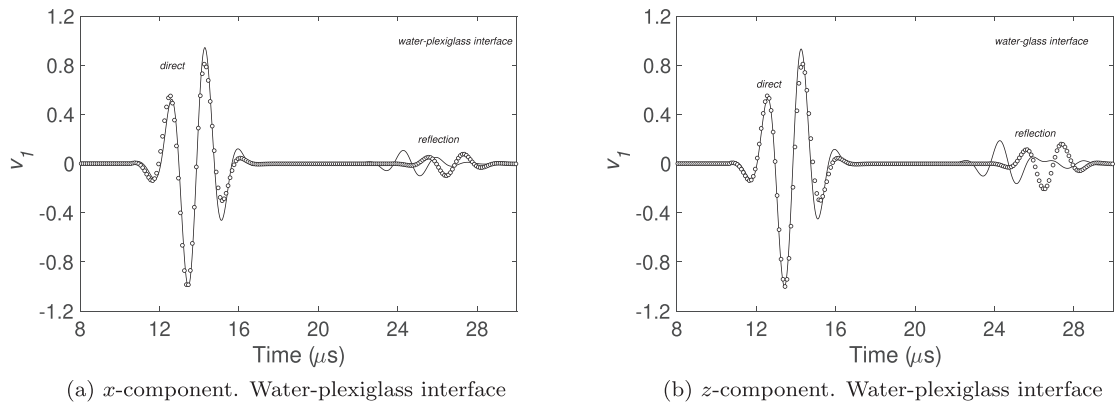


FIG. 6. Implicit boundary condition: Simulation of the reflection response using the Lax-Friedrich (inconsistent) flux, where the solid line and circles correspond to the numerical and analytical solutions, respectively. The figure represents the normalized particle-velocity components corresponding to water-plexiglass (a) and water-glass (b). Source and receiver are located in the fluid at 0.0158831 m above the interface and are separated by 0.016 m . The source is an explosion ($f_{11} = f_{33}$), with a central frequency of 500 kHz .

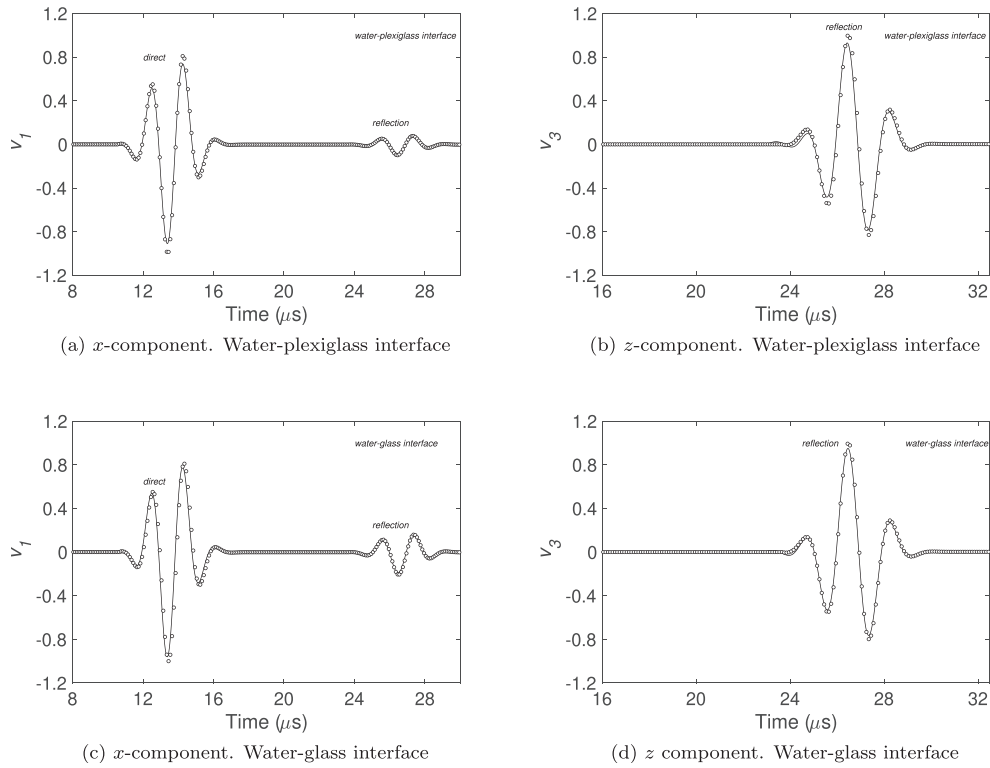


FIG. 7. Implicit boundary-condition: Simulation of the reflection response using the penalized consistent central flux, where the solid line and circles correspond to the numerical and analytical solutions, respectively. The figure shows the normalized particle-velocity components corresponding to water-plexiglass (a and b) and water-glass (c and d). Source and receiver are located in the fluid at 0.0158831 m above the interface, and are separated by 0.016 m. The source is an explosion, ($f_{11} = f_{33}$) with a central frequency of 500 kHz.

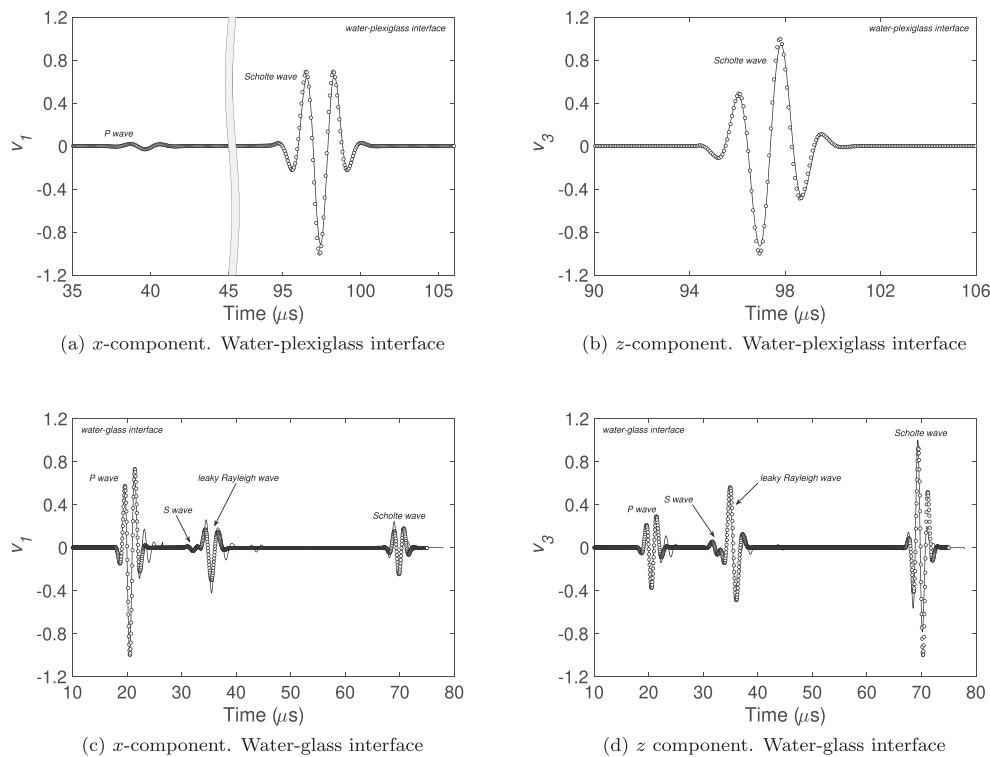


FIG. 8. Implicit boundary-condition: Simulation of interface-waves using a penalized consistent central flux, where the solid line and dots correspond to the numerical and analytical solutions, respectively. The figure shows the normalized particle-velocity components corresponding to water-plexiglass (a and b) and water-glass (c and d). Source and receiver are both located in the solid at 38.4 μm below the interface, with a separation 0.1 m. The source is an explosion ($f_{11} = f_{33}$), with a central frequency of 500 kHz.

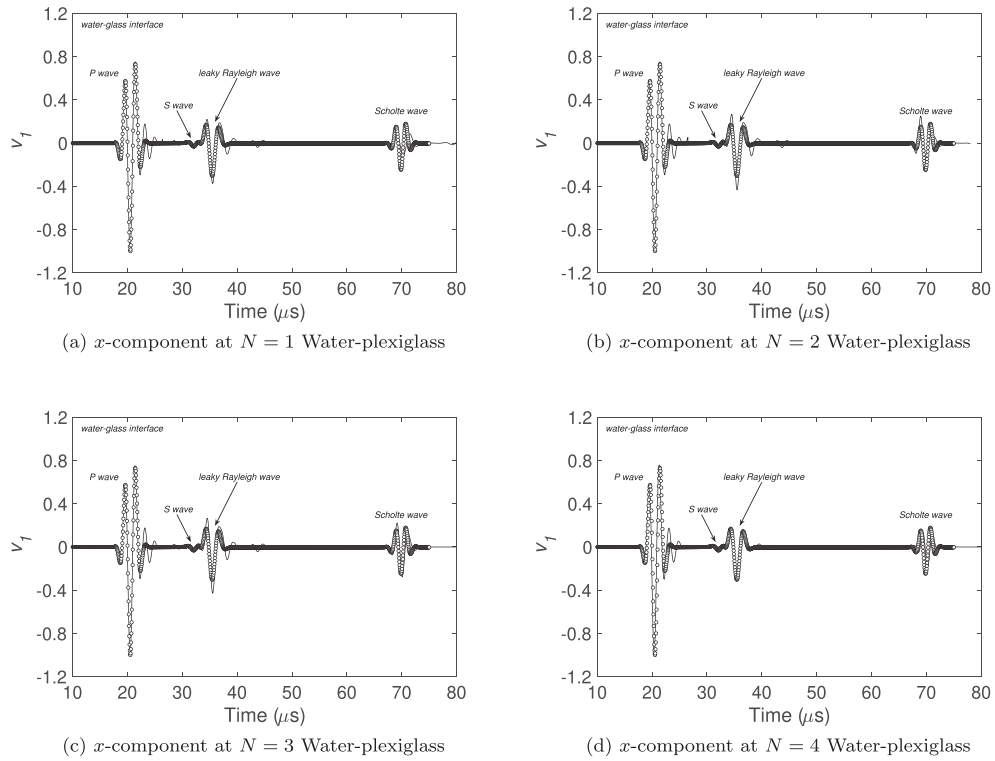


FIG. 9. Comparison of x - component of particle velocity computed at different polynomial degrees (N). Figures 9(a)–9(d) show the comparison of solution for $N=1, 2, 3$, and 4. The solid line and dots correspond to the numerical and analytical solutions, respectively. It should be noted that the numerical solution converges to analytical solutions as N increases.

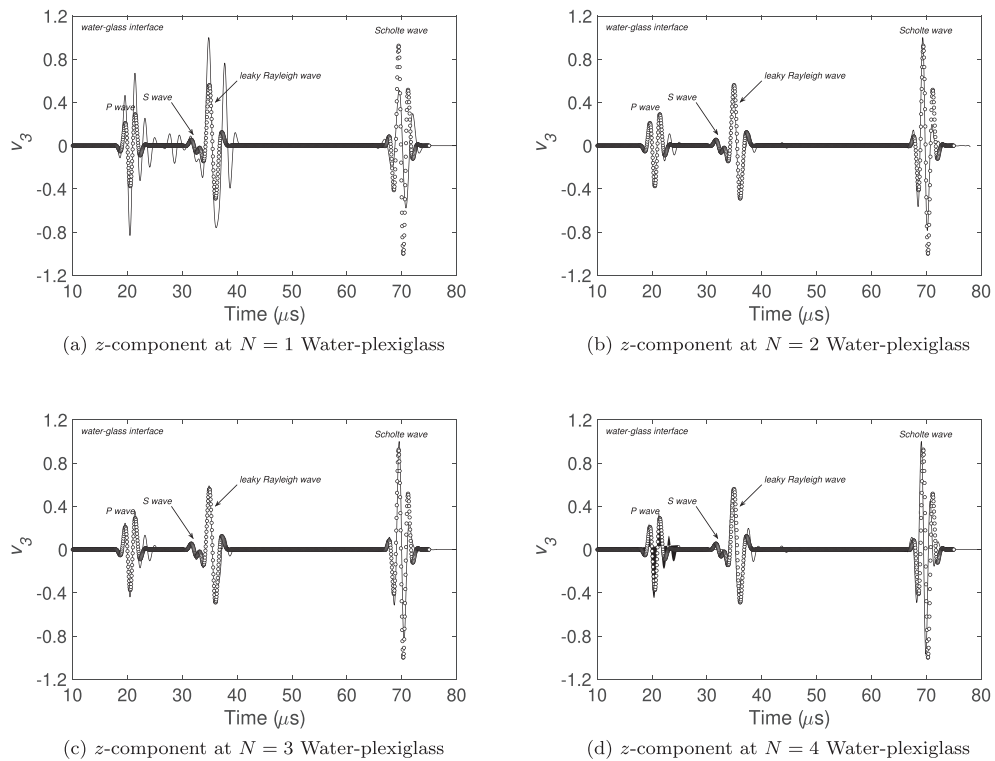


FIG. 10. Comparison of z - component of particle velocity computed at different polynomial degrees (N). The solid line and dots correspond to the numerical and analytical solutions, respectively. Figures 10(a)–10(d) show the comparison of solution for $N=1, 2, 3$, and 4. It is to be noted that the numerical solution converges to the analytical solutions as N increases.

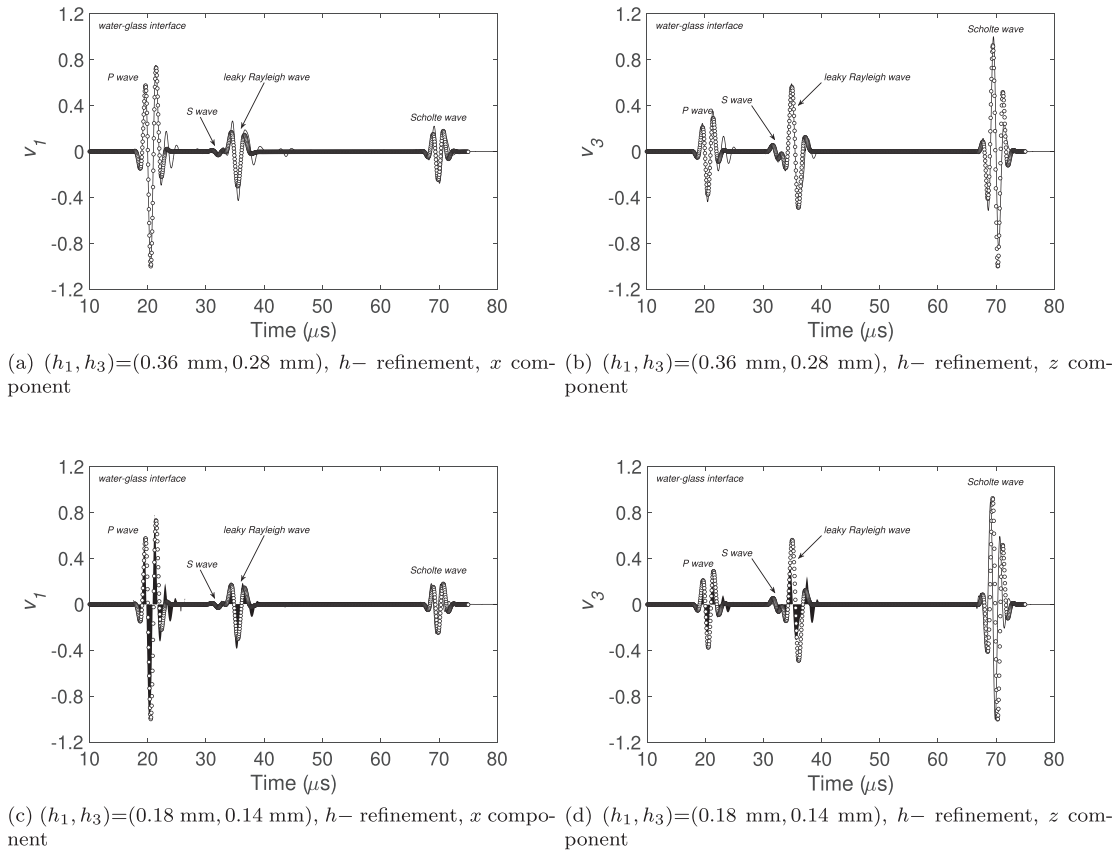


FIG. 11. Comparison of the analytical and numerical solution of particle velocities, computed after refining the mesh size. Figures 11(a) and 11(b) represent the solutions for coarse mesh, whereas Figs. 11(c) and 11(d) are at finer mesh. The solid line and circles correspond to the numerical and analytical solutions, respectively. It is to be noted that interface wave modes are more accurately modeled with finer mesh computation.

the x_1 and x_3 components of the normalized particle-velocity corresponding to the water-glass model, respectively. The direct and reflection modes are marked in the figures. The agreement between numerical and analytical solutions for both models is very good.

Next, we verify the ability of the numerical scheme to model interface waves. Source and receiver are both located in the solid at 38.4 mm with an offset of 0.1 m. The discretization parameters are the same as used in Fig. 4. Figures 5(a) and 5(b) show a comparison of the x and z components

of the normalized particle velocities for the water-plexiglass model (soft solid), respectively. The solutions show a very good agreement. The dominance of the Scholte wave in both components is clearly observed. A comparison of the analytical and numerical solutions for the water-glass model (stiff solid) is shown in Figs. 5(c) and 5(d). The agreement between the solutions of v_1 is very good, whereas the same level of agreement is not observed for v_3 . A discussion about improving the convergence between analytical and numerical solutions is included below. However, the presence of

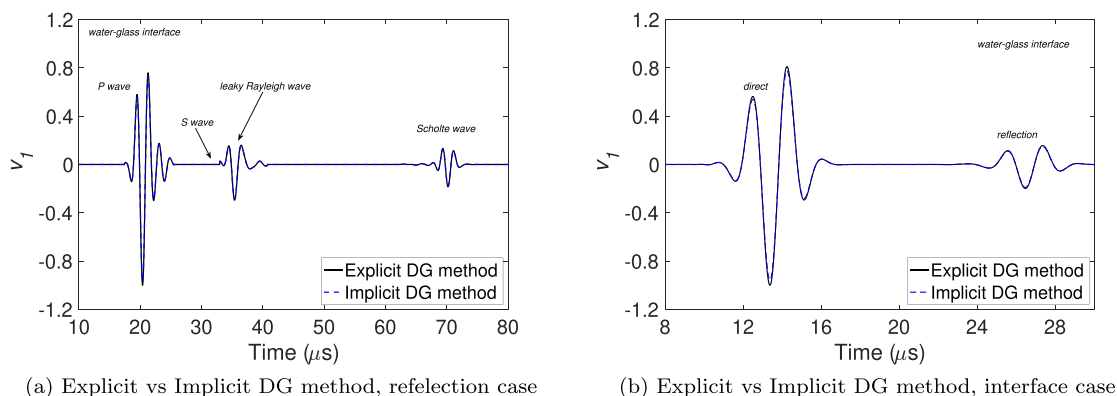


FIG. 12. (Color online) Comparison of numerical solutions obtained from explicit and implicit dG methods and pseudo-spectral methods where (a) and (b) represent the comparison x component of particle velocity (v_1) of glass for interface and reflection wave modes.

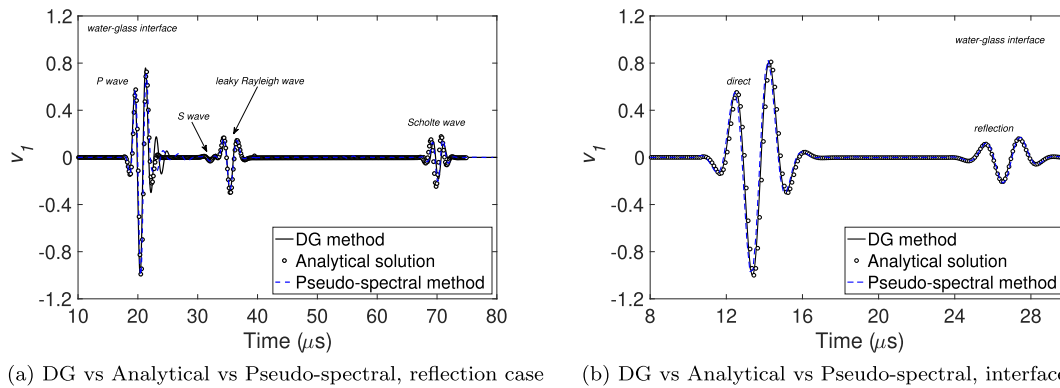


FIG. 13. (Color online) Comparison of numerical solutions obtained from dG method and pseudo-spectral method (Carcione et al., 2018) against the analytical solution, where (a) and (b) represent the comparison of x component of particle velocity (v_1) of glass for reflection and interface wave modes.

the leaky Rayleigh and Scholte waves is clearly observed, along with the P and S waves, marked clearly in Figs. 5(c) and 5(d).

Next, we show the ability of the implicit numerical scheme with Lax-Friedrich flux [Eq. (41)] and setting the $\mu = 0$. Figures 6(a) and 6(b) show a comparison between the numerical and analytical solutions of the particle velocities for the water-plexiglass and water-glass models, respectively. It is clear that the reflection mode is not accurately simulated by the scheme. This results from the fact that the scheme is not consistent.

Now, we show results of the numerical scheme using the implicit numerical scheme (based on the penalty fluxes) expressed in Eqs. (47) and (48). Figures 7 and 8 show the comparison of the analytical and numerical solutions for the reflection and interface problems. The discretization parameters and source-receiver geometry are the same as those used for the results shown in Figs. 4 and 5. Figures 7 and 8 show a good agreement between the numerical and analytical solutions for the body (P and S waves) and interface waves, with the same accuracy observed in the explicit case. Results from the implicit case also confirm that the implicit implementation of boundary condition in numerical scheme is accurate, provided a consistent flux is used.

The comparison of the numerical and analytical solutions for the water-glass interface is fairly accurate for v_3 as shown in Fig. 5(d). To analyze this further, additional numerical solutions of v_1 and v_3 are computed, first by refining the degree of the polynomial, N (p -refinement) and then by decreasing the mesh size (h -refinement). Figures 9 and 10 represent the refinement of the numerical solution of v_1 and v_3 for $N = 1 - 4$ with a mesh size of 0.37 and 0.56 mm in the x_1 and x_3 directions, respectively. Figures 9(a)–9(d) represent v_1 for $N = 1 - 4$ and show that the agreement between the analytical and numerical solutions improves with N . The L_2 -error between the analytical and numerical solutions decreases from 0.00467% ($N = 1$) to 0.0018% ($N = 4$). Figure 10 shows the comparison between the numerical and analytical solutions of v_3 for $N = 1 - 4$. Figure 10 clearly indicates that the accuracy increases with N as the L_2 -error decreases from 0.00587% ($N = 1$) to 0.0038% ($N = 4$).

Next, we consider the h -refinement and show the comparison between analytical and numerical solutions of v_1 and v_3 for the water-glass interface. In Figs. 11(a) and 11(b), the numerical solutions of v_1 and v_3 are computed with $N = 3$ and mesh sizes $h_1 = 0.36$ mm and $h_3 = 0.56$ mm, respectively. The refinement of the solution of v_1 and v_3 is further done with the mesh sizes $h_1 = 0.18$ mm and $h_3 = 0.28$ mm, shown in Figs. 11(c) and 11(d), respectively. Comparing Figs. 11(a) and 11(c) clearly shows that the leaky-Rayleigh and Scholte waves are more accurately modeled with finer mesh sizes. The amplitude of the Scholte wave in the v_3 component is more accurately captured with a finer mesh size [Fig. 11(d)] than those in Figs. 11(b) and Fig. 5(d), where the analytical solution overshoots the numerical solutions. The mesh refinement results in the decrease of the L^2 -error (in v) from 0.0016 to 1.965×10^{-4} with an order of 3.65 and confirms with the convergence rate of the dG method, i.e., $O(h^{N+1})$ (Hesthaven and Warburton, 2007).

Next, we validate the numerical solutions obtained from explicit and implicit dG methods. Figures 12(a) and 12(b) show the v_1 and v_3 components of the particle velocity for water-glass interface. The solutions are computed with a polynomial of degree $N = 3$ and mesh size (0.18 and 0.14 mm) with 3.8×10^6 degrees of freedom. Figures 12(a) and 12(b) compare the v_1 components, computed for the interface and reflection case in a water-glass setup. The L^2 -error between the implicit and explicit schemes are 0.037% and 0.0266%, corresponding to the interface [Fig. 12(a)] and reflection cases [Fig. 12(b)], respectively.

Finally, Fig. 13 shows a comparison between the analytical and numerical solutions obtained from a dG and a pseudo-spectral methods (Carcione et al., 2018). The discretization parameters used for the dG method are the same as those used in Fig. 12. Figures 13(a) and 13(b) clearly support that the solutions obtained from all methods are in very good agreement.

VII. CONCLUSIONS

We present analytical and numerical results of waves propagating at the fluid-solid interface for two solids: plexiglass

(soft) and glass (stiff). To perform the numerical simulations, we use a dG method with upwind (explicit method) and penalty fluxes (implicit method) to implement the correct boundary conditions. We show that setting the rigidity in the fluid equal to zero in the dG formulation yields the wrong results. The numerical solution obtained from upwind and penalty flux based methods are correct for the complete set of waves, i.e., including the Scholte and leaky-Rayleigh waves. The comparison of the numerical solutions and the analytical solutions shows a very good agreement. This test is essential to verify the correct simulation of wave propagation in the presence of fluid-solid interfaces, corresponding to soft and stiff solid bottoms.

ACKNOWLEDGMENTS

K.S. would like to thank Dr. Ruichao Ye, ExxonMobil, Houston, TX, for his time to discuss the penalty flux and its implementation in the dG formulation. The authors would like to thank BP America, Houston, TX, for discussions and guidance on the topic. This research was conducted using computational resources and services at the Center for Computation and Visualization, Brown University. K.S. would like to acknowledge Dr. Helen Kershaw from CCV, Brown University, for providing the help and feedback at various stages of the research, especially for problems concerning to the computation.

Ansell, J. H. (1972). "The roots of the stoneley wave equation for solid-liquid interfaces," *Pure Appl. Geophys.* **94**(1), 172–188.

Ash, E. A., and Paige, E. G. (1985). *Rayleigh-Wave Theory and Application: Proceedings of An International Symposium Organised by the Rank Prize Funds at the Royal Institution, London, 1985* (Springer-Verlag, Berlin).

Berg, P., If, F., Nielsen, P., and Skovgaard, O. (1994). "Analytical reference solutions," in *Modeling The Earth For Oil Exploration*, edited by K. Helbig (Pergamon Press, London), pp. 421–427.

Cagniard, L. (1962). *Reflection and Refraction of Progressive Seismic Waves, Translation and Revision of Cagniard, L., 1939, Réflexion et Réfraction des Ondes Séismiques Progressives* (McGraw-Hill, New York).

Carbajal-Romero, M., Flores-Mendez, E., Flores-Guzmán, N., Núñez-Farfán, J., Olivera-Villaseñor, E., and Sánchez-Sesma, F. J. (2013). "Scholte waves on fluid-solid interfaces by means of an integral formulation," *Geofísica Inter.* **52**(1), 21–30.

Carcione, J. M. (2014). *Wave Fields in Real Media. Theory and Numerical Simulation of Wave Propagation in Anisotropic, Anelastic, Porous and Electromagnetic Media, 3rd edition* (Elsevier, Amsterdam, the Netherlands).

Carcione, J. M., Bagaini, C., Ba, J., Wang, E., and Vesnaver, A. (2018). "Waves at fluid–solid interfaces: Explicit versus implicit formulation of the boundary condition," *Geophys. J. Int.* **215**(1), 37–48.

Carcione, J. M., and Helle, H. B. (2004). "The physics and simulation of wave propagation at the ocean bottom/wave propagation at ocean bottom," *Geophysics* **69**(3), 825–839.

Chaljub, E., Capdeville, Y., and Vilotte, J.-P. (2003). "Solving elastodynamics in a fluid–solid heterogeneous sphere: A parallel spectral element approximation on non-conforming grids," *J. Comput. Phys.* **187**(2), 457–491.

Chan, J. (2018). "Weight-adjusted discontinuous Galerkin methods: Matrix-valued weights and elastic wave propagation in heterogeneous media," *Int. J. Numer. Methods Eng.* **113**(12), 1779–1809.

Cockburn, B., and Shu, C.-W. (2001). "Runge–Kutta discontinuous Galerkin methods for convection-dominated problems," *J. Sci. Comput.* **16**(3), 173–261.

De Basabe, J. D., and Sen, M. K. (2014). "A comparison of finite-difference and spectral-element methods for elastic wave propagation in media with a fluid-solid interface," *Geophys. J. Int.* **200**(1), 278–298.

de Hoop, A. T., and Van der Hijden, J. H. (1983). "Generation of acoustic waves by an impulsive line source in a fluid/solid configuration with a plane boundary," *J. Acoust. Soc. Am.* **74**(1), 333–342.

Farnell, G. (1970). "Properties of elastic surface waves," *Phys. Acoust.* **6**, 109–166.

Glorieux, C., Van de Rostyne, K., Gusev, V., Gao, W., Lauriks, W., and Thoen, J. (2002). "Nonlinearity of acoustic waves at solid–liquid interfaces," *J. Acoust. Soc. Am.* **111**(1), 95–103.

Glorieux, C., Van de Rostyne, K., Nelson, K., Gao, W., Lauriks, W., and Thoen, J. (2001). "On the character of acoustic waves at the interface between hard and soft solids and liquids," *J. Acoust. Soc. Am.* **110**(3), 1299–1306.

Guo, K., Acosta, S., and Chan, J. (2019). "A weight-adjusted discontinuous galerkin method for wave propagation in coupled elastic-acoustic media," [arXiv:1905.09145](https://arxiv.org/abs/1905.09145).

Hesthaven, J. S., and Warburton, T. (2007). *Nodal Discontinuous Galerkin Methods: Algorithms, Analysis, and Applications* (Springer Science & Business Media, New York).

Komatitsch, D., Barnes, C., and Tromp, J. (2000). "Wave propagation near a fluid-solid interface: A spectral-element approach," *Geophysics* **65**(2), 623–631.

Madec, R., Komatitsch, D., and Diaz, J. (2009). "Energy-conserving local time stepping based on high-order finite elements for seismic wave propagation across a fluid-solid interface," *Comput. Model. Eng. Sci.* **14**(2), 163.

Padilla, F., de Billy, M., and Quentin, G. (1999). "Theoretical and experimental studies of surface waves on solid–fluid interfaces when the value of the fluid sound velocity is located between the shear and the longitudinal ones in the solid," *J. Acoust. Soc. Am.* **106**(2), 666–673.

Rauch, D. (1980). "Experimental and theoretical studies of seismic interface waves in coastal waters," in *Bottom-Interacting Ocean Acoustics* (Springer, New York), pp. 307–327.

Scholte, J. (1942). "On the stoneley wave equation," *Proc. Koninklijke Nederlandse Akademie van Wetenschappen* **45**, 20–25.

Shukla, K., Chan, J., de Hoop, M. V., and Jaiswal, J. (2020). "A weight-adjusted discontinuous Galerkin method for the poroelastic wave equation: Penalty fluxes and micro-heterogeneities," *J. Comput. Phys.* **403**(1), 109061–109094.

Stephen, R. (1983). "A comparison of finite difference and reflectivity seismograms for marine models," *Geophys. J. Int.* **72**(1), 39–57.

van Vossen, R., Robertsson, J. O., and Chapman, C. H. (2002). "Finite-difference modeling of wave propagation in a fluid-solid configuration," *Geophysics* **67**(2), 618–624.

Warburton, T. (2013). "A low-storage curvilinear discontinuous galerkin method for wave problems," *SIAM J. Sci. Comput.* **35**(4), A1987–A2012.

Wilcox, L. C., Stadler, G., Burstedde, C., and Ghattas, O. (2010). "A high-order discontinuous Galerkin method for wave propagation through coupled elastic–acoustic media," *J. Comput. Phys.* **229**(24), 9373–9396.

Ye, R., de Hoop, M. V., Petrovitch, C. L., Pyrak-Nolte, L. J., and Wilcox, L. C. (2016). "A discontinuous Galerkin method with a modified penalty flux for the propagation and scattering of acousto-elastic waves," *Geophys. J. Int.* **205**(2), 1267–1289.

Zhang, J. (2004). "Wave propagation across fluid-solid interfaces: A grid method approach," *Geophys. J. Int.* **159**(1), 240–252.